ACES Asian Chemical Editorial Society

DOI: 10.1002/cnma.201600259

CHEMNANOMAT
Full Paper

## Electrode Materials

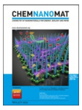

# Hierarchical Hybrids of Mesoporous $NiCo_2O_4$ Needles/Graphene/Carbon Nanotubes with High Performance for Lithium Ion Batteries and Oxygen Reduction Reactions

Yan Yan,[a] Yuqing Liu,[a] Weiyan Ni,[a] Jinyan Wu,[a] Mingkai Liu,*[a] and Tianxi Liu*[a, b]

**Abstract:** Three-dimensional (3D) hierarchical $NiCo_2O_4$-graphene/carbon nanotube (NiCo-G/CNT) hybrids with $NiCo_2O_4$ needles deposited on a conductive G/CNT template have been facilely produced by a co-precipitation method. Mesoporous $NiCo_2O_4$ needles endow the NiCo-G/CNT hybrids with high specific surface area, which allows good electrolyte penetration and large electrode–electrolyte contact area, leading to fast ion and electron transfer and excellent strain accommodation. The unique hierarchical structures of NiCo-G/CNT hybrids ensure complete exposure of their active sites and endow them with dual functionalities that allow them to serve as high-performance electrodes for both lithium-ion batteries and oxygen reduction reactions. In particular, the NiCo4-G/CNT sample delivers a remarkable specific capacitance of 1392 $mAh\,g^{-1}$ at current density of 0.1 $A\,g^{-1}$, and achieves high electrocatalytic activity with long-term stability for ORR. This preparation strategy is simple and effective, and can be conveniently extended to fabricate other kinds of binary-oxide-based materials for energy-storage applications.

## Introduction

The global energy crisis and harsh environmental issues have sharply increased over the past decades due to the depletion of fossil fuels and inefficient usage of recycled resources.[1–3] In addition, global warming and excessive resource consumption make it necessary for human society to develop new and renewable energy systems with excellent performance as well as multifunctional energy-storage abilities.[4,5] Renewable energy storage systems including solar cells, lithium-ion batteries (LIBs), supercapacitors, etc. have drawn much research attention due to their unique properties such as high specific capacitance, long-term cycling stability, low cost, environmental friendliness, as well as large-scale production capacity.[6,7] It should be noted that superior energy conversion and storage systems are constructed based on high-performance active electrode materials with hierarchical interior structures.

Up to now, numerous active materials have been investigated in order to boost the potential abilities in energy conversion and storage, among which developing high-performance electrode materials with high energy density and good cyclability are of great significance. As one of the most famous active materials, binary metal oxides (e.g., nickel cobalt oxide, cobalt aluminum oxide, and cobalt iron oxide) with higher theoretical capacity have been recognized as promising alternative anode materials.[8–10] In particular, spinel nickel cobaltite ($NiCo_2O_4$) materials with unique characteristics, including low cost, high natural abundance, high specific capacity, especially good electronic conductivity and electrochemical activity, have been distinguished as excellent anode electrode materials.[11] These prominent features endow $NiCo_2O_4$-based materials with desirable prospects for their applications in electrochemical energy-storage fields.[12] In addition, hierarchical porous nanostructured materials with high surface area can meet the demand of thorough immersion of electrolyte and complete exposure of their active sites. However, fatal drawbacks of $NiCo_2O_4$, such as large volume changes and stresses, usually cripple its efficiency during lithium ion insertion/extraction processes, resulting in aggregation of active materials and severe pulverization of electrodes.[13] Those disadvantages cause a great increase in the interfacial contact resistance and significant capacity fading during long-term cycling, which seriously limits the future commercial applications of these $NiCo_2O_4$ active materials as well as other binary metal oxides.

Much effort has been devoted to solving the problems above. One effective strategy is to hybridize the binary metal

---

[a] *Dr. Y. Yan, Y. Liu, W. Ni, J. Wu, Dr. M. Liu, Prof. T. Liu*
*School of Chemistry and Chemical Engineering*
*Jiangsu Key Laboratory of Green Synthetic Chemistry for Functional Materials*
*Jiangsu Normal University*
*No.101, Shanghai Road, Xuzhou, Jiangsu 221116 (P.R.China)*
*E-mail: liumingkai@jsnu.edu.cn*
*txliu@dhu.edu.cn*

[b] *Prof. T. Liu*
*State Key Laboratory for Modification of Chemical Fibers and Polymer Materials*
*College of Materials Science and Engineering*
*Donghua University*
*2999 North Renmin Road, Shanghai 201620 (P.R. China)*

*Supporting information for this article can be found under http://dx.doi.org/10.1002/cnma.201600259.*

oxides with a conductive matrix such as nickel foam, carbon fiber films, graphene sheets, etc. The conductive matrix can not only prevent the severe aggregation of binary metal oxides, but can effectively accelerate the rapid transfer of electrons, achieving reduced volume expansion during long-term cycling. Unfortunately, graphene sheets are prone to becoming tightly restacked due to the strong "π–π" interfacial reaction, and nickel foam and carbon fiber films possess low specific surface area, resulting in lower energy density of the devices.[14] Three-dimensional (3D) carbonic materials with ultra-light weight and high surface area are promising substrates for loading active materials to improve their electrochemical performance, and also make an additional contribution to the total energy-storage ability.[15–18] Moreover, 3D carbonic matrices decorated with active nanomaterials with abundant porous structures can further ensure efficient contact between the electrolyte and active materials, achieving better utilization of their active sites. Furthermore, most $NiCo_2O_4$-based hybrid materials in previous reports were synthesized by hydrothermal or solvothermal methods, which have drawbacks for mass production.[19] Thus, it will be of great importance to develop effective methods for growing mesoporous active binary metal oxide materials on a 3D conductive carbonic matrix with rapid transfer of ions and electrons to give anode electrode materials for energy-storage devices.

In this work, mesoporous $NiCo_2O_4$ needles deposited on 3D carbonic graphene/carbon nanotube (G/CNT) templates were prepared and used as anode electrode materials for LIBs. By bonding CNTs between different graphene sheets, 3D G/CNT can successfully prevent the interfacial aggregation propensity of graphene, at the same time accelerating the formation of porous structures. With these porous G/CNTs as a deposition matrix, $NiCo_2O_4$ needles can be orderly and vertically arranged on their surface, avoiding serious aggregation and fully exposing their active sites to lithium ions. Acting as anode materials, the obtained $NiCo_2O_4$-graphene-carbon nanotube (NiCo-G/CNT) hybrids exhibit remarkably improved specific capacity (1392 $mA\,h\,g^{-1}$) and long-term cycling stability (87% retention after 100 cycles) compared with pure $NiCo_2O_4$ nanocrystals. Furthermore, desirable electrocatalytic activity and long-term durability of these NiCo-G/CNT hybrids have been achieved as a result of the excellent catalytic activity of $NiCo_2O_4$ needles and good electrical conductivity of the G/CNT matrix. These distinct features make NiCo-G/CNT hybrids promising candidates for possible applications in energy-storage fields.

## Results and Discussion

The preparation process is schematically illustrated in Figure 1. First, pristine CNTs with bundle morphologies were added into a graphene oxide dispersion with ultrastrong stirring and mild sonication. During this treatment, CNT bundles can be thoroughly dispersed by large graphene oxide sheets due to the intense interfacial "π–π" interaction.[20] When the graphene oxide sheets were chemically reduced by $HI{\cdot}H_2O$, the inserted pristine CNTs can further hinder their tight interfacial stacking, resulting in good porous structures inside the G/CNT sheets.

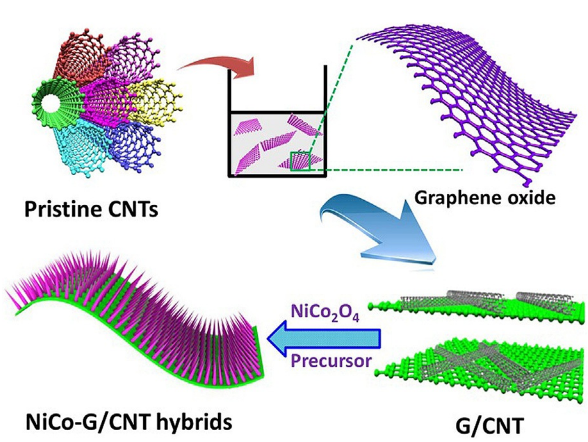

**Figure 1.** Schematic illustration of fabrication process of 3D NiCo-G/CNT hybrids with $NiCo_2O_4$ needles deposited on conductive G/CNT templates.

Precursors of $NiCo_2O_4$ needles were uniformly anchored on the surface of G/CNT composite via a urea-assisted chemical co-precipitation process, and 3D NiCo-G/CNT hybrids with hierarchical structures can be obtained after careful annealing treatment.

Figure 2 shows the SEM images of pristine CNTs (a), G/CNT composite (b), NiCo-G/CNT hybrids with different mole ratios (c–h) and pure $NiCo_2O_4$ microspheres (i). Pristine CNTs show tube-like structures with lengths in micrometers, as seen in Figure 2a. After being co-dispersed by graphene oxide sheets, the CNTs were uniformly dispersed and tightly bonded on the surface of graphene sheets in the G/CNT composite (Figure 2b). NiCo1-G/CNT hybrid, with 1 mmol $Ni^{2+}$, 2 mmol $Co^{2+}$ and a certain amount of urea as the precursor, shows the apparent existence of $NiCo_2O_4$ needles on the surface of G/CNT composite (Figure 2c). Then, with the increase of the precursor, more and more $NiCo_2O_4$ needles can be observed in the hybrids of NiCo2-G/CNT (Figure 2d), NiCo3-G/CNT (Figure 2e),

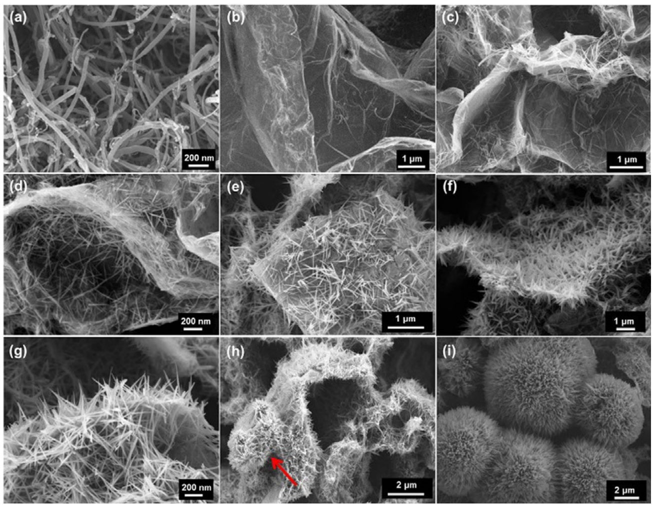

**Figure 2.** SEM images of prepared samples: (a) pristine CNTs, (b) G/CNT composite, (c) NiCo1-G/CNT hybrid, (d) NiCo2-G/CNT hybrid, (e) NiCo3-G/CNT hybrid, (f and g) NiCo4-G/CNT hybrid at low and high magnifications, (h) NiCo5-G/CNT hybrid with aggregated $NiCo_2O_4$ microspheres, (i) pure $NiCo_2O_4$ microspheres.

and NiCo4-G/CNT (Figure 2 f and 2 g). Interestingly, $NiCo_2O_4$ needles in NiCo2-G/CNT and NiCo3-G/CNT hybrids were still lying on the surface of G/CNT, due to the lack of sufficient $NiCo_2O_4$ needles. When the precursors of $Ni^{2+}$ and $Co^{2+}$ were increased to 4 times, individual $NiCo_2O_4$ needles were deposited on the surface of the G/CNT matrix with porous structures. Thus, the active sites of $NiCo_2O_4$ needles can be totally exposed to electrolyte and lithium ions with retention of the compact interfacial contact between $NiCo_2O_4$ needles and conductive G/CNT substrate. The enlarged SEM image at high magnification of NiCo4-G/CNT hybrid (Figure 2 g) can be further used for the illustration of their 3D hierarchical structures with $NiCo_2O_4$ needles deposited on G/CNT template. The pores and voids inside NiCo4-G/CNT hybrid are beneficial for electrolyte infiltration, while tightly connected G/CNT enables fast electron and ion transportation.[21] However, when the amount of $Ni^{2+}$ and $Co^{2+}$ was increased 5 fold, unexpected huge aggregation of $NiCo_2O_4$ needles into pure $NiCo_2O_4$ microspheres (Figure 2 h) was observed, as indicated by the arrow. This unwanted aggregation of $NiCo_2O_4$ needles can reduce the specific surface area of active NiCo5-G/CNT hybrid, even shielding some active sites inside the aggregates, resulting in the undesired decrease in their electrochemical performance. Moreover, pure $NiCo_2O_4$ materials exhibit a spherical morphology with a larger size (Figure 2 i) resulting from the heavy aggregation of the $NiCo_2O_4$ needles without the assistance of the G/CNT template. The chemical compositions of NiCo4-G/CNT hybrid were further analyzed by EDS (Figure 3). Elemental mappings corresponding to Co, Ni, O, and C obviously demonstrate the uniform dispersion of $NiCo_2O_4$ on G/CNT substrate. Furthermore, the obtained EDS spectrum confirms that the atomic ratio of Co and Ni was approximately 2:1 and no other element was introduced into the NiCo-G/CNT hybrids.

The crystallographic phase of NiCo-G/CNT samples and pure $NiCo_2O_4$ nanospheres was identified by XRD, as seen in Figure S1 in the Supporting Information. Six well-defined diffraction peaks at $2\theta = 18.8^\circ$, $31.1^\circ$, $36.7^\circ$, $44.6^\circ$, $59.1^\circ$, $65.0^\circ$ can be observed, which can be indexed to the lattice plane of (111), (220), (311), (400), (511), and (440) of the spinel $NiCo_2O_4$, respectively.[22,23] XRD result obviously confirms the formation of $NiCo_2O_4$ crystallites (according to JCPDS No. 20-0781) on the surface of G/CNT template.[24,25] The intensity of the crystal peaks was gradually increased, as seen in Figure S1 a–e, which is consistent with the $NiCo_2O_4$ needles content increasing in NiCo-G/CNT samples.

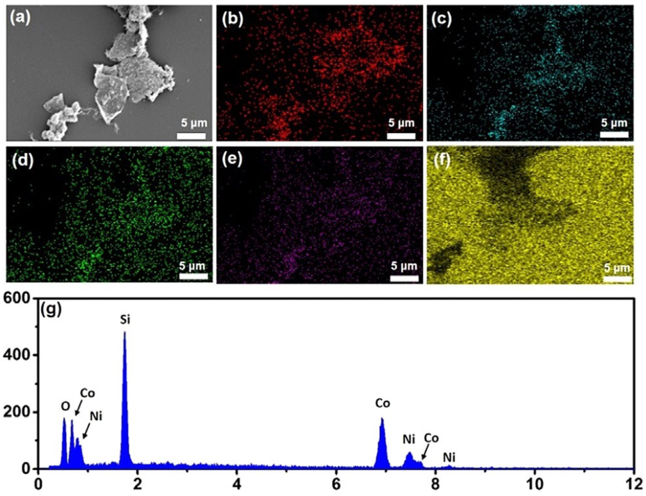

**Figure 3.** (a) SEM image of NiCo4-G/CNT, and corresponding EDS mappings results from (b) Co, (c) Ni, (d) O, (e) C elements, and (f) silicon substrate, as well as (g) energy spectrum of NiCo4-G/CNT.

More detailed information of structural and morphological features of the prepared NiCo-G/CNT hybrids and pure $NiCo_2O_4$ nanocrystals was further obtained by TEM, as seen in Figure 4. TEM images of NiCo-G/CNT hybrids with low content of $NiCo_2O_4$ (Figure 4 a–4 c) clearly present the needle morphology of $NiCo_2O_4$ nanocrystals which are tightly bound on the surface of large-scale G/CNT substrates. Figure 4 d and 4 e show the TEM images of NiCo4-G/CNT hybrid at low and high magnifications. A great number of $NiCo_2O_4$ needles were homogeneously deposited on G/CNT without any aggregation (Figure 4 d), and acicular $NiCo_2O_4$ bundles with typical diameter of 30–50 nm for each $NiCo_2O_4$ needle can be further observed in the enlarged TEM image (Figure 4 e). However, when the amounts of $NiCo_2O_4$ precursors were increased to 5 mmol ($Ni^{2+}$) and 10 mmol ($Co^{2+}$), the obtained NiCo5-G/CNT hybrid shows aggregated structures due to the excessive $NiCo_2O_4$ content. The TEM image (Figure 4 g) of pure $NiCo_2O_4$ shows the microsphere morphology, which is consistent with their SEM images (Figure 2 i). The high-resolution TEM image (Figure 4 h and 4 i) of NiCo4-G/CNT presented two types of lattice fringes with interplanar spacings of 0.47 and 0.25 nm, corresponding to the (111) and (311) planes of the spinel $NiCo_2O_4$ phase, which is consistent with the characteristic diffraction peaks obtained by the XRD pattern discussed above.

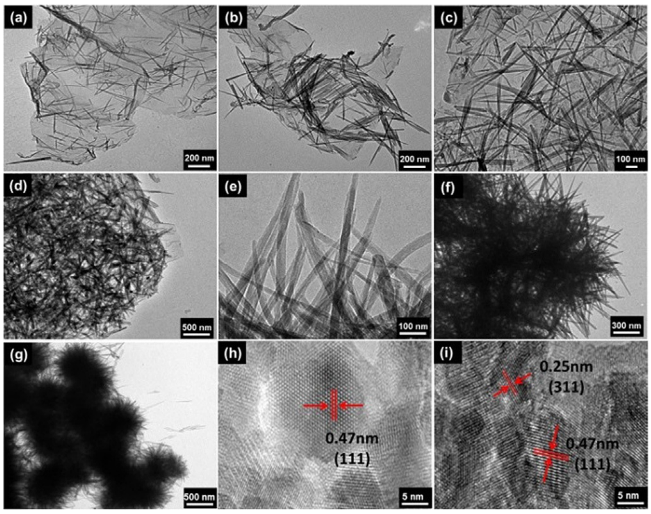

**Figure 4.** TEM images and crystal lattice plane of prepared samples: (a) NiCo1-G/CNT hybrid, (b) NiCo2-G/CNT hybrid, (c) NiCo3-G/CNT hybrid, (d and e) NiCo4-G/CNT hybrid at low and high magnifications, (f) NiCo5-G/CNT hybrid with partial aggregation, (g) pure $NiCo_2O_4$ nanocrystals, (h and i) HRTEM images of $NiCo_2O_4$ needles on NiCo4-G/CNT.

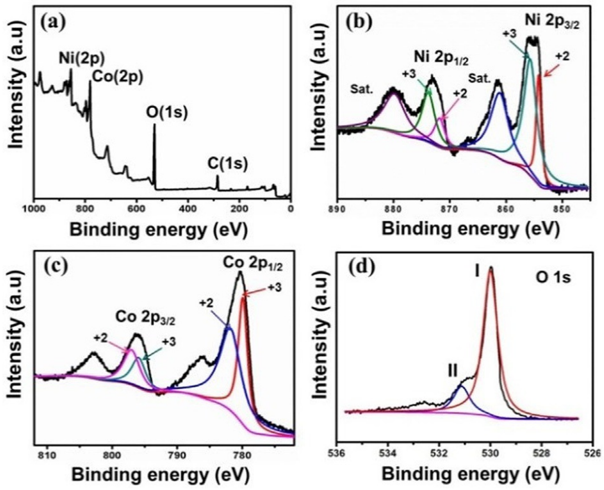

**Figure 5.** XPS spectra of NiCo4-G/CNT hybrid: (a) full-range survey and (b) high-resolution of Ni 2p, (c) Co 2p and (d) C 1s spectra.

The chemical compositions of NiCo4-G/CNT hybrid were further analyzed by XPS in the range of 0–1000 eV, as shown in Figure 5. The general survey spectrum presented in Figure 5a indicates the NiCo4-G/CNT hybrid consists of C, Ni, Co, O elements without any other impurities. Two prominent peaks at binding energy of 853.4 and 872.5 eV observed in the Ni 2p spectrum (Figure 5b) can be attributed to the $2p_{3/2}$ and $2p_{1/2}$ spin-orbit of Ni element in NiCo4-G/CNT hybrid.[26] Simultaneously, two shake-up satellites can also be found in Ni 2p spectrum (identified as "Sat"), consistent with the XPS results of familiar $NiCo_2O_4$ crystals.[27] The Co 2p spectrum was also fitted with two spin-orbit doublets according to a Gaussian fitting method, indicating the existence of Co $2p_{3/2}$ and Co $2p_{1/2}$ spin-orbit peaks. These results demonstrate that the Ni and Co elements in NiCo4-G/CNT hybrid exist as $Ni^{2+}$, $Ni^{3+}$, $Co^{2+}$, and $Co^{3+}$, respectively, which are in good agreement with the results of pure $NiCo_2O_4$.[13,28] Three oxygen contributions were observed from the high-resolution spectrum for the O 1s region (Figure 5d). Specifically, the main peak at about 530.0 eV is typical of the O–Co/Ni bonds, and the peak at 531.3 is usually associated with the defects with low oxygen coordination in the materials such as hydroxyls, chemisorbed oxygen and under-coordinated lattice oxygen.[21] Furthermore, the broad peak at ~532.8 eV can be attributed to multiplicity of physically and chemically sorbed water molecules on their surface.[29]

The porosity and pore size distribution of prepared samples were investigated by BET analysis. Figure 6 shows the nitrogen adsorption–desorption isotherms and the Barrett–Joyner–Halenda (BJH) pore size distribution plots (inset) of the prepared NiCo-G/CNT hybrids. The isotherm can be fitted well to a typical IV isotherm with H3 hysteresis loops in the relative pressure range of 0.5–0.95, indicating the presence of mesoporous structures inside the prepared NiCo-G/CNT hybrids. The specific surface areas of the prepared samples obtained from the BET analysis are about 87, 97, 126, 196, 166 and 108 $m^2g^{-1}$ for NiCo1-G/CNT, NiCo2-G/CNT, NiCo3-G/CNT, NiCo4-G/CNT, NiCo5-G/CNT and pure $NiCo_2O_4$ nanosphere. The best result (196 $m^2g^{-1}$) of NiCo4-G/CNT is higher than recently reported results of $NiCo_2O_4$-based active materials.[19,30] Furthermore, the pore size distribution analysis (inset spectra in Figure 6d) of NiCo4-G/CNT indicates that most of the pores fall into the size range of 3–9 nm with an average value of 7 nm. Compared with the result of pure $NiCo_2O_4$ nanosphere, the greatly enhanced specific surface area of NiCo4-G/CNT can be ascribed to the successful interfacial deposition of $NiCo_2O_4$ needles on porous G/CNT template, which rejects any aggregation tendency of $NiCo_2O_4$ nanocrystals inside the NiCo-G/CNT hybrids. Moreover, the formation of the mesopores might be due to the gas releasing during decomposition of $NiCo_2O_4$ precursor synthesized with urea as capping agent.[31] Large specific surface area and porous features are beneficial for the electrochemical performance of active electrodes by offering more active sites within the pores for fast and complete electrochemical reactions, which can further facilitate the rapid transfer of lithium ions and electrons at the electrolyte/active material interface.[19,32] These structural features can make a contribution to the lithium-ion storage properties of NiCo-G/CNT hybrids.

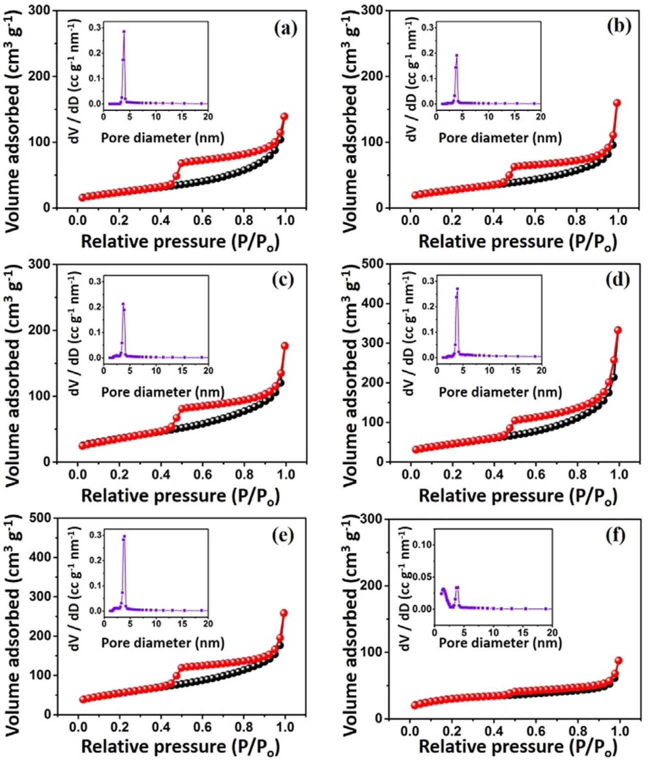

**Figure 6.** Nitrogen adsorption–desorption isotherms of NiCo-G/CNT hybrids, (a) NiCo1-G/CNT, (b) NiCo2-G/CNT, (c) NiCo3-G/CNT, (d) NiCo4-G/CNT, (e) NiCo5-G/CNT, and (f) pure $NiCo_2O_4$ microspheres. Inset shows the corresponding Barrett–Joyner–Halenda (BJH) pore size distribution of each sample.

A series of electrochemical measurements were carried out in order to investigate the electrochemical performance of the prepared NiCo-G/CNT hybrids and pure $NiCo_2O_4$ microspheres.

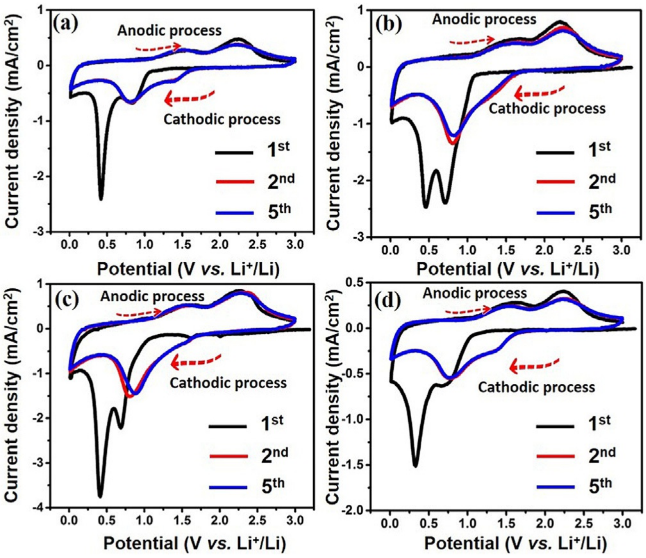

**Figure 7.** CV curves of (a) NiCo1-G/CNT, (b) NiCo4-G/CNT, (c) NiCo5-G/CNT hybrids, and (d) pure $NiCo_2O_4$ crystals for the 1st, 2nd, and 5th cycles at a scan rate of 0.1 $mV\,s^{-1}$ in the voltage range of 0.01–3.0 V vs. $Li^+/Li$.

Figure 7 shows the CV curves of NiCo1-G/CNT hybrid, NiCo4-G/CNT hybrid, NiCo5-G/CNT hybrid, and pure $NiCo_2O_4$ microspheres at a scan rate of 0.1 $mV\,s^{-1}$ over the voltage range of 0.01–3.0 V vs. $Li^+/Li$. Lithium ion insertion and extraction reactions can be expressed as the following equations according to the previously reported Li storage mechanism in $NiCo_2O_4$-based active materials:[21,33]

$$NiCo_2O_4 + 8\,Li^+ + 8\,e^- \rightarrow Ni + 2\,Co + 4\,Li_2O \qquad (1)$$

$$Ni + Li_2O \rightarrow NiO + 2\,Li^+ + 2\,e^- \qquad (2)$$

$$2\,Co + 2\,Li_2O \rightarrow 2\,CoO + 4\,Li^+ + 4\,e^- \qquad (3)$$

$$3\,CoO + Li_2O \rightarrow Co_3O_4 + 2\,Li^+ + 2\,e^- \qquad (4)$$

A large irreversible cathodic peak located at around 0.45 V was observed in all the CV curves of NiCo-G/CNT hybrids and pure $NiCo_2O_4$ microspheres, which can be ascribed to the electrochemical $Li^+$ insertion reaction that occurs by reducing $NiCo_2O_4$ to metallic Ni and Co according to Equation (1).[13] Meanwhile, two well-defined peaks at about 1.5 and 2.2 V during the anodic process were due to the electrochemical extraction of lithium ions in the active electrode materials by oxidation of $Ni^0$ and $Co^0$ to $Ni^{2+}$ and $Co^{3+}$ [Eqs. (2)–(4)]. NiCo1-G/CNT hybrid shows similar anodic and cathodic peaks like those of NiCo4-G/CNT and pure $NiCo_2O_4$ microspheres with such a low content of $NiCo_2O_4$, indicating good electrochemical activities of incorporated $NiCo_2O_4$ needles. Furthermore, in the second and fifth lithiation cycles, the reduction peaks shifted to 0.9 V compared to the first cycle with an obvious decline of peak intensity in both anodic and cathodic processes, indicating a different redox behavior occurs in the first cycle.[34] Here, the peak intensity and integrated area of CV curves of NiCo4-G/CNT hybrid (Figure 7a) are much larger than other samples, confirming its maximum capacitance with a proper mole ratio of $NiCo_2O_4$ needles and G/CNT matrix. In particular, the larger cathodic peak at 0.75 V (vs. $Li^+/Li$) of NiCo4-G/CNT hybrid compared with the others further confirms their better porosity. The smaller integrated CV area of NiCo5-G/CNT hybrid compared with that of NiCo4-G/CNT is a result of the inevitable aggregation by interfacial deposition of excessive $NiCo_2O_4$ nanomaterials. It is worth noting that the CV curves obtained in the 2nd and 5th cycles for the NiCo4-G/CNT hybrid show barely any changes in the intensity of the peaks and integrated area, which means their electrochemical performance was stable in the subsequent cycles.

The galvanostatic charge/discharge profiles of NiCo1-G/CNT, NiCo4-G/CNT, and pure $NiCo_2O_4$ microspheres at a current density of 0.1 $A\,g^{-1}$ in the range of 0.01 and 3.0 V are presented in Figure 8a, 8b and 8c, respectively. All of the three discharge–charge profiles contain a wide and steady potential plateau from 1.0 to 0.5 V in the first discharge process, followed by a gradual voltage decrease. The initial specific capacities of NiCo1-G/CNT, NiCo4-G/CNT, and pure $NiCo_2O_4$ microspheres obtained from the first discharge curve were about 1286, 1857, and 896 $mA\,h\,g^{-1}$, respectively, which are much higher than the capacities obtained from the subsequent discharge curves. Here, the capacity loss at the first discharge can be ascribed to the formation of a solid electrolyte interphase (SEI),[35,36] and the potential plateaus in the subsequent discharge curves shifted to the higher voltage (~1.0 V, vs. $Li^+/Li$) due to the irreversible reaction of $NiCo_2O_4$ and lithium ions, as illustrated by Equation (1). Apparent potential plateaus at ~1.5 V vs. $Li^+/Li$ and ~2.3 V vs. $Li^+/Li$ were obtained in the charge curves of NiCo1-G/CNT, NiCo4-G/CNT, and pure $NiCo_2O_4$ microspheres, and are consist with the anodic peaks in their CV curves, which can be attributed to different electrochemical reactions according to Equation (2), Equation (3) and Equation (4), respectively.[14] The NiCo1-G/CNT, NiCo4-G/CNT, and pure $NiCo_2O_4$ microspheres deliver a specific capacity of 845, 1392, and 707 $mA\,h\,g^{-1}$, respectively, with Coulombic efficiency of 65.7%, 74.9% and 78.9%. The large irreversible capacity loss after the first cycle can be ascribed to the uncompleted decomposition of the SEI film,[37] because this passivation layer may increase the diffusional resistance and block the utilization of the interior active materials. The tiny difference between the 2nd and 5th discharge–charge curves of NiCo1-G/CNT and NiCo4-G/CNT hybrids can further confirm their good reversible capability, which are consistent with the CV detection results. Interestingly, the high specific capacity (1392 $mA\,h\,g^{-1}$) of NiCo4-G/CNT outperforms most of the previously reported $NiCo_2O_4$-based active electrode materials (detailed comparisons are provided in Table 1), confirming the favorable cooperation between $NiCo_2O_4$ needles with porous G/CNT templates. Here, the high capacity of the nanowire arrays resulted from their thoroughly exposed active sites and the fast electron transfer ability of the Ni foam and G/CNT templates. Unfortunately, pure $NiCo_2O_4$ microspheres show large capacity loss in the 5th cycle compared with that in the 2nd cycle, indicating irreversible electrochemical reactions occur during their long-term cycling.

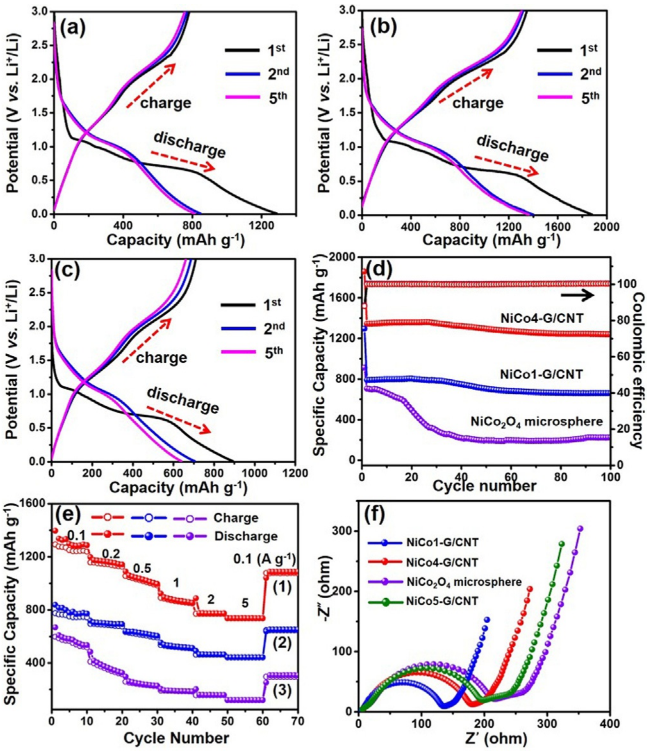

**Figure 8.** Electrochemical performance of prepared NiCo-G/CNT hybrids and pure $NiCo_2O_4$ microspheres. Charge/discharge curves for the 1st, 2nd, and 5th cycles for (a) NiCo1-G/CNT, (b) NiCo4-G/CNT, and (c) pure $NiCo_2O_4$ microspheres at the current density of 0.1 $A\,g^{-1}$. (d) Cycling performance of NiCo1-G/CNT, NiCo4-G/CNT, pure $NiCo_2O_4$ microspheres and the corresponding Coulombic efficiency for NiCo4-G/CNT. (e) Rate capability of (1) NiCo4-G/CNT, (2) NiCo1-G/CNT and (3) pure $NiCo_2O_4$ microspheres at various current densities (0.1 to 5 $A\,g^{-1}$) (f) Nyquist plots of NiCo1-G/CNT, NiCo4-G/CNT, NiCo5-G/CNT and pure $NiCo_2O_4$ microspheres measured with an amplitude of 10 mV over the frequency range from 100 kHz to 0.01 Hz.

**Table 1.** Comparison of the lithium-ion storage ability between NiCo4-G/CNT and $NiCo_2O_4$-based materials reported previously.

| Materials | Morphology | Synthesis method | Capacity [$mA\,h\,g^{-1}$] | Ref. |
|---|---|---|---|---|
| $NiCo_2O_4$/Ni foam | Nanowire arrays | Hydrothermal | 1520 (at 0.1 $A\,g^{-1}$) | [27] |
| NiCo4-G/CNT | Nanoneedles | Co-precipitation | 1392 (at 0.1 $A\,g^{-1}$) | This work |
| $NiCo_2O_4$/graphene | Nanosheet | Hydrothermal | 1372 (at 0.1 $A\,g^{-1}$) | [4] |
| $NiCo_2O_4$@Au | Nanotubes | Electrospinning/calcination | 1315 (at 0.1 $A\,g^{-1}$) | [2] |
| $NiCo_2O_4$ | Microspheres | Hydrothermal | 1260 (at 0.1 $A\,g^{-1}$) | [37] |
| $NiCo_2O_4$ | Hollow nanospheres | Co-precipitation | 1210 (at 0.2 $A\,g^{-1}$) | [38] |
| $NiCo_2O_4$ | Hollow nanocubes | Etching/precipitation | 1160 (at 0.2 $A\,g^{-1}$) | [30] |
| $NiCo_2O_4$ | Porous flower | Hydrothermal | 1146 (at 0.1 $A\,g^{-1}$) | [32] |
| $NiCo_2O_4$/3DHPC | Nanoparticles | Hydrothermal | 1046 (at 0.1 $A\,g^{-1}$) | [29] |
| $NiCo_2O_4$-RGO | Nanoplates | Hydrothermal | 974 (at 0.1 $A\,g^{-1}$) | [24] |
| $NiCo_2O_4$ | Microflowers | Solvothermal | 952 (at 0.1 $A\,g^{-1}$) | [26] |

Good long-term cycling stability is pivotal for excellent electrodes in LIBs. Figure 8d shows the charge/discharge cycling performance of NiCo1-G/CNT, NiCo4-G/CNT, and pure $NiCo_2O_4$ microspheres at a current density of 0.1 $A\,g^{-1}$ between 0.01 and 3.0 V. In the first cycle, all the three active materials exhibit ultrahigh discharge capacity but possess low Coulombic efficiency. Interestingly, from the second cycle, NiCo1-G/CNT and NiCo4-G/CNT hybrids exhibit gradually increasing capacities. This phenomenon can be ascribed to the reversible formation of a polymeric gel-like film originating from the slow kinetic activation of cobalt-based active materials.[19,35] However, pure $NiCo_2O_4$ microspheres suffer a severe decrease by 30 cycles, which was caused by the deficient electron transportation inside the $NiCo_2O_4$ microspheres, resulting in the destruction and collapse of their internal structures.[38] From the 30th cycle, the charge/discharge capacities of NiCo1-G/CNT and NiCo4-G/CNT show very slow fading and reversible capacities of 661 and 1240 $mA\,h\,g^{-1}$ can be retained after 100 cycles, corresponding to 83.1 % and 92.2 % of their capacities in the second cycle. The pure $NiCo_2O_4$ microspheres show much faster capacity fading with only 31.7 % (224 $mA\,h\,g^{-1}$) capacity retention after 100 cycles. Here, the greatly enhanced cycling stability of NiCo1-G/CNT and NiCo4-G/CNT hybrids compared to pure $NiCo_2O_4$ microspheres was attributed to the fact that volume variations upon long-term cycling can be effectively buffered and the electrons can be rapidly transferred with the assistance of 3D porous G/CNT matrix, giving rise to their excellent cycling stabilities. Long-term cycling up to 500 times of NiCo4-G/CNT hybrids was also observed, as seen in Figure S2. The capacity fading occurred in the first 100 cycles, but extraordinary stability was obtained from 100 to 500 cycles, coupled with a high Coulombic efficiency of about 100 %. Also, the minimal difference between charge/discharge curves at the 2nd and 500th cycles (Figure S3) is also strong evidence to confirm their good cycling stability.

The rate performance of NiCo1-G/CNT, NiCo4-G/CNT, and pure $NiCo_2O_4$ microspheres at different current densities ranging from 0.1 to 5 $A\,g^{-1}$ were also evaluated to investigate their high-power performance in LIBs, as seen in Figure 8e. NiCo1-G/CNT and NiCo4-G/CNT hybrids exhibit excellent cycling performance at different current densities apart from the first four cycles. The irreversible capacity loss during the initial cycles was caused by the decomposition of the electrolyte and/or solvent.[22] NiCo-G/CNT hybrids exhibit outstanding rate capabilities compared to $NiCo_2O_4$ microspheres with average discharge capacities of 1289, 1167, 1032, 884, and 778 $mA\,h\,g^{-1}$ for NiCo4-G/CNT hybrid at current densities of 0.1, 0.2, 0.5, 1.0, and 2.0 $A\,g^{-1}$, respectively. Even at a high current density of 5 $A\,g^{-1}$, NiCo4-G/CNT and NiCo1-G/CNT hybrids still delivered reversible capacities of 734 and 440 $mA\,h\,g^{-1}$, which are much higher than 123 $mA\,h\,g^{-1}$ of the pure $NiCo_2O_4$ microspheres. Interestingly, when the current density reversed back to a low current density of 0.1 $A\,g^{-1}$, the discharge capacities of NiCo4-G/CNT and NiCo1-

G/CNT hybrids return to 1105 and 671 mA h g$^{-1}$ accordingly, nearly recovering to their initial values. In contrast, the pure $NiCo_2O_4$ microsphere electrode shows worse rate performance with quick decrease of its capacities as the current density increases. The significant difference in rate performances between NiCo-G/CNT hybrids and pure $NiCo_2O_4$ may result from the efficient incorporation of conductive G/CNT matrix with rapid electron transfer inside the NiCo-G/CNT hybrids. The excellent rate performance as well as the good long-term cycling stability renders the NiCo-G/CNT hybrids very promising candidates for LIB electrodes.

In order to further understand the superior electrochemical performance of NiCo-G/CNT hybrids, electrochemical impedance spectroscopy (EIS) analysis of NiCo-G/CNT hybrids and pure $NiCo_2O_4$ microspheres were conducted. Figure 8 f shows the Nyquist plots of NiCo1-G/CNT, NiCo4-G/CNT, NiCo5-G/CNT hybrids and pure $NiCo_2O_4$ microspheres in the frequency from 100 kHz to 0.01 Hz in a fully charged state. Here, the Nyquist plots are derived from the contributions of both anode and cathode materials. Due to the same anode electrode material of ideal lithium metal sheet, the differences in the Nyquist plots are mainly induced by the different cathode materials. All the Nyquist plots exhibit two depressed semicircles in high and medium frequency regions, and Warburg behaviors at low frequency region. Semicircle diameters of NiCo1-G/CNT and NiCo4-G/CNT hybrids are smaller than pure $NiCo_2O_4$ microspheres, indicating their decreased charge-transfer resistance in the electrolyte/electrode interface ($R_{ct}$). Intersection points on the real axis in high frequency of NiCo1-G/CNT, NiCo4-G/CNT, NiCo5-G/CNT hybrids and $NiCo_2O_4$ microspheres are 3.15, 4.94, 5.01 and 7.99 Ω, which represent their electrolyte resistance ($R_e$).[19] Here, sample NiCo5-G/CNT exhibits almost the same Nyquist plot as pure $NiCo_2O_4$ microspheres due to its heavy loading of $NiCo_2O_4$ needles outside, and also confirms its decreased specific capacity compared with sample NiCo4-G/CNT. Also, straight lines in the low frequency region can be observed in the Nyquist plots of NiCo1-G/CNT and NiCo4-G/CNT hybrids, corresponding to the Warburg behavior that resulted from the solid-state diffusion of lithium ions into the bulk active electrode materials.[35] The greatly decreased resistance values of NiCo1-G/CNT and NiCo4-G/CNT hybrids result from the assistance of the G/CNT template, and further contribute to their excellent electrochemical performance.

The superior electrochemical performance of NiCo-G/CNT hybrids can be attributed to their special architectures; the thorough diffusion of lithium ions and fast electron transfer inside NiCo-G/CNT hybrids are schematically shown in Figure 9. First, $NiCo_2O_4$ needles deposited on carbon matrix provides a large surface area and perfect dispersion rather than heavy aggregation, achieving full exposure of their active sites to lithium ions. Second, the open geometry of NiCo-G/CNT hybrids ensures easy penetration of electrolyte ions into their inner regions, and the mesoporous architecture of the $NiCo_2O_4$ needles also provides sufficient space for the volume expansion during the discharge/charge process. Last but not least, 3D conductive G/CNT networks acting as a deposition template make it possible for the rapid and timely transportation of electrons, contributing to the enhanced electrochemical performance of NiCo-G/CNT hybrids compared to pure $NiCo_2O_4$ microspheres.

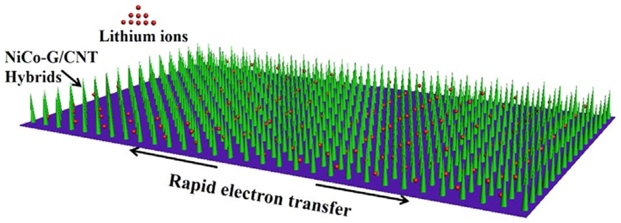

**Figure 9.** Schematic representation of thorough diffusion of electrolyte ions and rapid electron transfer throughout the NiCo-G/CNT hybrids.

Furthermore, NiCo4-G/CNT hybrids were used as an electrochemical catalyst to boost their activities in oxygen reduction reaction (ORR) applications. Cyclic voltammetry (CV) measurements of NiCo4-G/CNT hybrid were performed in $O_2$-saturated and $N_2$-saturated KOH electrolyte (0.1 м) at room temperature, as seen in Figure 10 a. NiCo4-G/CNT catalyst shows a pure capacitive current background in $N_2$-saturated electrolyte, but achieves an apparent cathodic peak at −0.353 V vs. Ag/AgCl in $O_2$-saturated electrolyte. Also, the onset ORR potential at around −0.101 V vs. Ag/AgCl of NiCo4-G/CNT catalyst can further clearly confirm its good ORR catalytic activity. Here, the onset potential of each curve was obtained from the corresponding differential curve, as seen in Figure S4. This good catalytic performance towards oxygen molecules not only comes from the G/CNT matrix but also from the $NiCo_2O_4$ needles with a large number of active sites. Linear-sweep voltammetry (LSV)

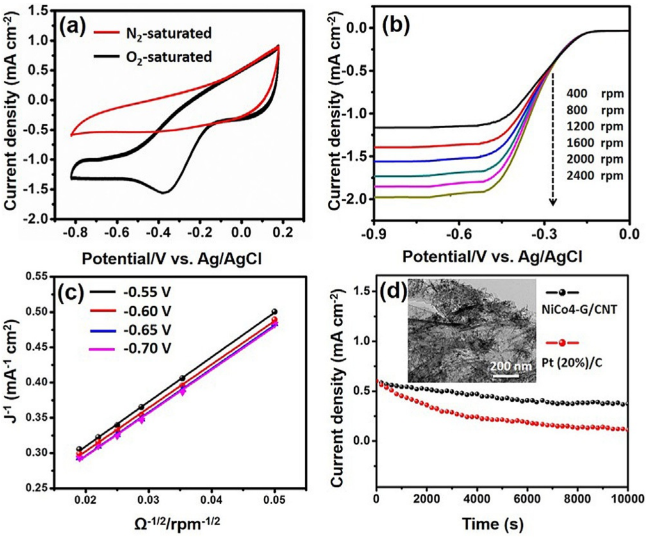

**Figure 10.** Electrocatalytic performance of NiCo4-G/CNT hybrid for oxygen reduction reaction: (a) CV curves in $N_2$-saturated and $O_2$-saturated KOH solution (0.1 м) on a glassy carbon electrode with a sweep rate of 100 mV s$^{-1}$. (b) RDE curves in $O_2$-saturated KOH solution at different rotating speeds from 400 to 2400 rpm with a sweep rate of 10 mV s$^{-1}$. (c) Koutecky–Levich plots ($j^{-1}$ vs. $w^{-1/2}$) at different potentials from −0.55 to −0.70 V from the RDE curves. (d) Corresponding chronoamperometry curves of NiCo4-G/CNT hybrid and Pt(20 %)/C catalysts obtained at −0.4 V in $O_2$-saturated KOH (0.1 м). Inset: TEM image of NiCo4-G/CNT hybrid after 10 000 s for stability testing.

analysis based on rotating-disk electrode (RDE) measurements was also used to investigate the ORR kinetics and activity of NiCo4-G/CNT catalyst. Figure 10 b shows a set of LSV curves recorded from 400 to 2400 rpm of NiCo4-G/CNT hybrid. The measured current density was gradually enhanced with the increase of rotation rate due to the shorted diffusion distance at high rotation speeds. The ORR current density at 2400 rpm can reach $-0.097\ \mathrm{mA\,cm^{-2}}$ at $-0.353$ V and even $-1.9\ \mathrm{mA\,cm^{-2}}$ at the potential of $-0.8$ V vs. Ag/AgCl, which is comparable with previous reports.[39,40] Corresponding Koutecky–Levich plots ($J^{-1}$ vs. $\omega^{-1/2}$) can be obtained from the polarization curves at different potential values (Figure 10 c), and good linearity of the Koutecky–Levich plots as well as nearly parallelism of the fitting lines suggest the first-order reaction kinetics toward concentrated dissolved oxygen molecules,[41] and show a similar electron transfer number for ORR at different potentials. The transferred electron number ($n$) per $O_2$ calculated from the Koutecky–Levich equation is about 3.74 in the range from $-0.55$ to $-0.70$ V vs. Ag/AgCl, suggesting that the reduction of $O_2$ by NiCo4-G/CNT hybrid is dominated by a four-electron process, and the $O_2$ molecule has been directly reduced to $OH^-$.[42] Moreover, the durability of NiCo4-G/CNT hybrid and Pt(20 %)/C catalyst toward ORR was further evaluated with chronoamperometric measurements at $-0.4$ V in $O_2$-saturated KOH electrolyte (0.1 M). As seen in Figure 10 d, NiCo4-G/CNT hybrid lost only 18.9 % of its initial catalytic activity after 10 000 s compared with 40.7 % of Pt(20 %)/C. This good durable performance of NiCo4-G/CNT hybrid attests its exciting stability in alkaline solution, and further demonstrates its promising application prospects in fuel cells.

## Conclusions

In summary, hierarchical NiCo-G/CNT hybrids with mesoporous $NiCo_2O_4$ needles deposited on 3D conductive G/CNT template have been prepared through a cost-effective co-precipitation method. The porous structures of NiCo-G/CNT hybrids ensure thorough electrolyte immersion throughout the electrodes. With $NiCo_2O_4$ needles deposited on G/CNT template, their aggregation tendency has been efficiently restrained, and all of their active sites were fully utilized. Also, the large open space between neighboring $NiCo_2O_4$ needles provides sufficient space for their volume expansion during the long-term cycling, and further ensures every needle participates in the ultrafast electrochemical reactions. Furthermore, good electrical conductivity of the G/CNT template allows rapid transportation of electrons inside the NiCo-G/CNT hybrids. Benefiting from the well-defined structures, NiCo4-G/CNT hybrid achieves a reversible high specific capacitance of $1392\ \mathrm{mAh\,g^{-1}}$ at current density of $0.1\ \mathrm{A\,g^{-1}}$ with good cycling stability and excellent rate performance. More importantly, NiCo4-G/CNT hybrid thus prepared also exhibits excellent electrocatalytic activity and long-term stability for ORR. The method of vertically anchoring active composite materials on conductive templates is a promising route for the development of novel and stable binary oxides for various applications.

## Experimental Section

### Preparation of G/CNT composite

Pristine CNTs (100 mg) with diameter of 30–50 nm were added into graphene oxide dispersion ($1\ \mathrm{mg\,mL^{-1}}$, 200 mL) which is prepared according to a modified Hummers' method.[43] The mixed solution consisting of pristine CNTs and graphene oxide sheets was strongly stirred followed by high power sonication. Then, pristine CNTs could be thoroughly co-dispersed with graphene oxide, as described in our previous report.[19] Graphene oxide sheets in the obtained composite were partially reduced by $HI{\cdot}H_2O$ (2 mL, 55 wt %) at 80 °C, resulting in the formation of G/CNT composite (modified to $2\ \mathrm{mg\,mL^{-1}}$) after being washed with water and ethanol five times.

### Preparation of NiCo-G/CNT hybrids

The NiCo-G/CNT hybrids with needle-like $NiCo_2O_4$ on G/CNT template were synthesized via a urea-assisted chemical co-precipitation method. Typically, 1 mmol $Ni(NO_3)_2{\cdot}6\,H_2O$ (Aldrich), 2 mmol $Co(NO_3)_2{\cdot}6\,H_2O$ (Aldrich) and 24 mmol urea ($CON_2H_4$, 99.5 %, Aldrich) were dissolved in ultraclean water (50 mL) under vigorous stirring, forming a transparent pink solution. The obtained solution was poured into 60 mL of G/CNT composite dispersion and the mixture was further sonicated for 30 min after being strongly stirred for 1 h. Then, the mixture was heated to 90 °C in an oil bath for 6 h. The precipitates were collected through centrifugation and washed with ultraclean water after being cooled naturally. The synthesized products were then dried at 60 °C for 12 h, following by annealing treatment at 350 °C for 2 h in argon with a slow heating rate of $1\ ^{\circ}\mathrm{C\,min^{-1}}$, resulting in the formation of NiCo1-G/CNT hybrid. The amount of precursors ($Ni^{2+}$, $Co^{2+}$) for $NiCo_2O_4$ needles was increased by 2, 3, 4 and 5 times for the preparation of NiCo-G/CNT hybrids with different mole ratios, denoted as NiCo2-G/CNT, NiCo3-G/CNT, NiCo4-G/CNT, NiCo5-G/CNT, respectively. Pure $NiCo_2O_4$ microspheres were prepared with the same synthesis process without the addition of G/CNT template.

### Microstructural characterization

The microstructure and morphology of the samples coupled with energy dispersive spectroscopy (EDS) mappings were observed on a field emission scanning electron microscopy (FESEM, Zeiss ultra-55). Transmission electron microscopy (TEM) and high-resolution TEM (HRTEM) observations were performed with a JEOL JEM 2100 TEM under an acceleration voltage of 200 kV. X-ray photoelectron spectroscopy (XPS) analyses were performed on a PHI 5600 XPS system. The Brunauer–Emmett–Teller (BET) surface areas and pore-size distribution were conducted by nitrogen sorption/desorption at 77 K on a Quadrasorb SI-MP Surface Area and Porosity Analyzer (Quantachrome, America).

### Lithium ion insertion/extraction experiments

Electrochemical experiments on the lithium-ion storage ability of the samples were carried out in a two-electrode system with pure lithium sheet as the counter and reference electrode. The synthesized NiCo-G/CNT hybrids were uniformly mixed with carbon black and poly(vinylidene fluoride) (PVDF) with a weight ratio of 80:10:10. 1-Methyl-2-pyrrolidinone (NMP) was used as the solvent for preparing the slurries. The resulted slurries were coated on a copper foil and dried overnight under vacuum at 70 °C. 1:1 mixture of ethylene carbonate and dimethyl carbonate containing 1 M $LiPF_6$ was used as an electrolyte. The electrodes were roll pressed and the batteries were assembled in a glove-box filled with argon. Cyclic voltammogram (CV) curves were obtained with an ARBIN electrochemical working station (MSTAT-10 V/10 mA/48 Ch) in a potential range of 0.01 to 3.0 V (vs. Li$^+$/Li) at a scan rate of 0.1 mV s$^{-1}$. Charge and discharge measurements were performed on LAND 2001A battery testing systems. The specific capacity of each sample was calculated based on the active NiCo-G/CNT hybrids except for the mass of the binder and black carbon. The AC impedance measurements of prepared cells were carried out on a Solartron electrochemical interface analysis system (SI 1260, SI 1287) in the frequency range from 100 kHz to 0.01 Hz with amplitude of 10 mV.

### Oxygen reduction reaction experiments

The electrocatalytic activities of the samples were evaluated by CV and rotation disk electrode (RDE) techniques. The measurements were carried out in a 0.1 M KOH solution saturated by $O_2$ or $N_2$. A glassy carbon disk electrode (3 mm in diameter) was used for supporting the active materials, and the electrochemical active area is about 0.07065 cm$^2$. The catalyst suspension was prepared by dissolving 10 mg of NiCo-G/CNT hybrid in 3.84 mL ethanol and 160 µL 0.5 wt % Nafion solution, and then treated with ultrasonication for 30 min. The catalyst suspension was pipetted with a micropipettor on the surface of RDE, achieving a catalyst mass loading of 0.5 mg cm$^{-2}$. Here, the geometric area on the RDE is about 0.1256 cm$^2$. Ag/AgCl electrode and a Pt plate were used as the reference and counter electrodes, respectively. CV curves were recorded by applying a linear potential scan between −0.8 V and 0.2 V at a sweep rate of 50 mV s$^{-1}$. RDE measurements were carried out at different rotating speeds from 400 to 2400 rpm.

## Acknowledgements

This work was supported by the National Natural Science Foundation of China (No. 51125011 and 51433001), and Natural Science Foundation of Jiangsu Province (BK20150238), and the Project Funded by the Priority Academic Program Development of Jiangsu Higher Education Institutions.

**Keywords:** cobalt · lithium ion batteries · nickel · oxygen reduction reaction · porous structure

[1] L. Shen, L. Yu, X. Yu, X. Zhang, X. W. D. Lou, *Angew. Chem. Int. Ed.* **2015**, *54*, 1868–1872; *Angew. Chem.* **2015**, *127*, 1888–1892.
[2] J. Zhu, Z. Xu, B. Lu, *Nano Energy* **2014**, *7*, 114–123.
[3] G. Gao, H. B. Wu, X. W. D. Lou, *Adv. Energy Mater.* **2014**, *4*, 1400422.
[4] Y. Chen, J. Zhu, B. Qu, B. Lu, Z. Xu, *Nano Energy* **2014**, *3*, 88–94.
[5] G. Gao, H. B. Wu, S. Ding, X. W. D. Lou, *Small* **2015**, *11*, 432–436.
[6] J. Zhou, Y. Huang, X. Cao, B. Ouyang, W. Sun, C. Tan, Y. Zhang, Q. Ma, S. Liang, Q. Yan, H. Zhang, *Nanoscale* **2015**, *7*, 7035–7039.
[7] R. Alcántara, M. Jaraba, P. Lavela, J. L. Tirado, *Chem. Mater.* **2002**, *14*, 2847–2848.
[8] A. Pendashteh, J. Palma, M. Anderson, R. Marcilla, *J. Mater. Chem. A* **2015**, *3*, 16849–16859.
[9] F. Tu, J. Xie, S. Zhang, G. Cao, T. Zhu, X. Zhao, *J. Mater. Chem. A* **2015**, *3*, 5714–5721.
[10] C. Zhang, T. Kuila, N. H. Kim, S. H. Lee, J. H. Lee, *Carbon* **2015**, *89*, 328–339.
[11] T. Li, X. Li, Z. Wang, H. Guo, Y. Li, *J. Mater. Chem. A* **2015**, *3*, 11970–11975.
[12] W. Liu, T. Gao, Y. Yang, Q. Sun, Z. Fu, *Phys. Chem. Chem. Phys.* **2013**, *15*, 15806–15810.
[13] Y. Chen, M. Zhuo, J. Deng, Z. Xu, Q. Li, T. Wang, *J. Mater. Chem. A* **2014**, *2*, 4449–4456.
[14] L. Shen, Q. Che, H. Li, X. Zhang, *Adv. Funct. Mater.* **2014**, *24*, 2630–2637.
[15] Z. Fan, J. Yan, L. Zhi, Q. Zhang, T. Wei, J. Feng, M. Zhang, W. Qian, F. Wei, *Adv. Mater.* **2010**, *22*, 3723–3728.
[16] D. Yu, L. Dai, *J. Phys. Chem. Lett.* **2010**, *1*, 467–470.
[17] P. Chen, T. Xiao, Y. Qian, S. Li, S. Yu, *Adv. Mater.* **2013**, *25*, 3192–3196.
[18] Y. Yang, B. Wang, J. Zhu, J. Zhou, Z. Xu, L. Fan, J. Zhu, R. Podila, A. M. Rao, B. Lu, *ACS Nano* **2016**, *10*, 5516–5524.
[19] H. S. Jadhav, R. S. Kalubarme, C. Park, J. Kim, C. Park, *Nanoscale* **2014**, *6*, 10071–10076.
[20] C. Zhang, L. Ren, X. Wang, T. Liu, *J. Phys. Chem. C* **2010**, *114*, 11435–11440.
[21] J. Cheng, Y. Lu, K. Qiu, H. Yan, J. Xu, L. Han, X. Liu, J. Luo, J. Kim, Y. Luo, *Sci. Rep.* **2015**, *5*, 12099.
[22] Y. Zhu, J. Wang, Z. Wu, M. Jing, H. Hou, X. Jia, X. Ji, *J. Power Sources* **2015**, *287*, 307–315.
[23] M. U. Anu Prathap, C. Wei, S. Sun, Z. J. Xu, *Nano Res.* **2015**, *8*, 2636–2645.
[24] Y. Chen, B. Qu, L. Hu, Z. Xu, Q. Li, T. Wang, *Nanoscale* **2013**, *5*, 9812–9820.
[25] G. Huang, L. Zhang, F. Zhang, L. Wang, *Nanoscale* **2014**, *6*, 5509–5515.
[26] J. Xu, L. He, W. Xu, H. Tang, H. Liu, T. Han, C. Zhang, Y. Zhang, *Electrochim. Acta* **2014**, *145*, 185–192.
[27] G. Chen, J. Yang, J. Tang, X. Zhou, *RSC Adv.* **2015**, *5*, 23067–23072.
[28] W. Li, G. Li, J. Sun, R. Zou, K. Xu, Y. Sun, Z. Chen, J. Yang, J. Hu, *Nanoscale* **2013**, *5*, 2901–2908.
[29] L. Wang, L. Zhuo, C. Zhang, F. Zhao, *ACS Appl. Mater. Interfaces* **2014**, *6*, 10813–10820.
[30] H. Guo, L. Liu, T. Li, W. Chen, J. Liu, Y. Guo, Y. Guo, *Nanoscale* **2014**, *6*, 5491–5497.
[31] G. Zhang, X. W. D. Lou, *Adv. Mater.* **2013**, *25*, 976–979.
[32] L. Li, Y. Cheah, Y. Ko, P. Teh, G. Wee, C. Wong, S. Peng, M. Srinivasan, *J. Mater. Chem. A* **2013**, *1*, 10935–10941.
[33] L. Ma, X. Shen, H. Zhou, Z. Ji, K. Chen, G. Zhu, *Chem. Eng. J.* **2015**, *262*, 980–988.
[34] Q. Zhang, H. Chen, J. Wang, D. Xu, X. Li, Y. Yang, K. Zhang, *ChemSusChem* **2014**, *7*, 2325–2334.
[35] A. K. Mondal, D. Su, S. Chen, X. Xie, G. Wang, *ACS Appl. Mater. Interfaces* **2014**, *6*, 14827–14835.
[36] L. Hu, H. Zhong, X. Zheng, Y. Huang, P. Zhang, Q. Chen, *Sci. Rep.* **2012**, *2*, 986.
[37] J. Li, S. Xiong, Y. Liu, Z. Ju, Y. Qian, *ACS Appl. Mater. Interfaces* **2013**, *5*, 981–988.
[38] X. Yao, C. Zhao, J. Kong, D. Zhou, X. Lu, *RSC Adv.* **2014**, *4*, 37928–37933.
[39] G. Zhang, B. Y. Xia, X. Wang, X. W. D. Lou, *Adv. Mater.* **2014**, *26*, 2408–2412.
[40] S. Guo, S. Zhang, L. Wu, S. Sun, *Angew. Chem. Int. Ed.* **2012**, *51*, 11770–11773; *Angew. Chem.* **2012**, *124*, 11940–11943.
[41] M. Liu, Y. Song, S. He, W. W. Tjiu, J. Pan, Y. Xia, T. Liu, *ACS Appl. Mater. Interfaces* **2014**, *6*, 4214–4222.
[42] Y. Xiao, C. Hu, L. Qu, C. Hu, M. Cao, *Chem. Eur. J.* **2013**, *19*, 14271–14278.
[43] Z. Yang, H. Sun, T. Chen, L. Qiu, Y. Luo, H. Peng, *Angew. Chem. Int. Ed.* **2013**, *52*, 7545–7548; *Angew. Chem.* **2013**, *125*, 7693–7696.

Manuscript received: September 3, 2016
Accepted Article published: September 26, 2016
Final Article published: October 18, 2016